Preprint submitted to Journal of Materials Chemistry A and further published as *J. Mater Chem A., 2018, 6, 443.*

Comprehensive investigation of the lithium insertion mechanism of $Na_2Ti_6O_{13}$ anode material for Li-ion batteries

Alois Kuhn*,†, Juan Carlos Pérez-Flores†, Markus Hoelzel‡, Carsten Baehtz§, Isabel Sobrados#, Jesús Sanz# and Flaviano García-Alvarado†

† Facultad de Farmacia, Departamento de Química y Bioquímica, Urbanización Montepríncipe, Universidad CEU San Pablo, 28668 Boadilla del Monte, Madrid, Spain

‡ Forschungsneutronenquelle Heinz-Maier-Leibniz (FRM II), Technische Universität München, Lichtenbergstrasse 1, D-85747 Garching, Germany

§ Institute of Ion Beam Physics and Materials Research, Helmholtz-Zentrum Dresden-Rossendorf, D-01314 Dresden, Germany

Instituto de Ciencia de Materiales Madrid (CSIC), 28049 Cantoblanco, Madrid, Spain

KEYWORDS: Li insertion, $Na_2Ti_6O_{13}$ anode, structural changes, synchrotron XRD, neutron diffraction, Li mobility, NMR spectroscopy.

ABSTRACT

Sodium hexatitanate $Na_2Ti_6O_{13}$ with a tunnel structure has been proposed to be an attractive anode material for lithium ion batteries because of its low insertion voltage, structural stability and good reversibility. In order to obtain a full understanding of the properties of this titanate, a combination of in situ synchrotron X-ray diffraction, neutron diffraction and ^{7}Li MAS solid-state NMR spectroscopy is used in the present work. During the first insertion stage (centered at 1.3 V) lithium is allocated in square planar LiO_4 2*c* (Li1) sites, minimizing electrostatic repulsion with Na ions. During the second lithium uptake (centered at 1.1 V), Li ions pass from 2*c* to empty 4*i* (Li2) sites of y/b = 0.5 planes, near Ti^{3+} cations. Distribution of Li^+ and Na^+ ions with respect to Ti^{3+} cations was deduced from Fourier map differences (Rietveld technique) and NMR quantitative analyses in $LiNa_2Ti_6O_{13}$ and $Li_2Na_2Ti_6O_{13}$ samples. ^{7}Li MAS-NMR analysis showed that Li ions occupy three fourfold coordinated sites with reasonable Li^+-O-Ti^{3+} bond distances, while Na cations remain at eightfold coordinated positions near Ti^{4+} cations as deduced from ^{23}Na MAS-NMR spectroscopy. ^{7}Li MAS-NMR recorded at increasing temperatures suggests that Li ions move along sinusoidal paths to reduce Li-Na electrostatic interactions. Li mobility along the *b*-axis is favored by partial occupation of interstitial 4*i* sites (Li3) located at both sides of Na cations in y/b = 0 planes. In lithium inserted samples the most probable - Li1(2*c*) $\rightarrow$ Li3(4*i*) $\rightarrow$ Li1(2*c*) - conduction paths were deduced. However, formation of Li pairs at y/b=0 planes (Li2 sites), where Li ions are located near Ti^{3+} cations, reduce the amount of mobile Li ions that participate in conduction processes. Proximity of lithium to Li and Na ions limits insertion to ca. 2 Li ions per structural formula.

1. Introduction

Though graphite-based materials are desirable as anodes in LIBs in terms of energy density, formation of SEI film and lithium plating, owing to the low intercalation potential, may lead to serious safety concerns. The resulting growth of dendrites and internal short-circuits may end in rapid aging of the device, fire or explosion of the battery.[1-6] In this connection, the high potential titanium oxide-based anode materials with inherent high safety and chemical compatibility between electrode and electrolyte are expected to overcome these problems. When these materials are used in conjunction with high voltage cathodes[7-9] safer Li^+ ion systems are produced avoiding the risk of lithium dendrite formation.[10,11] $Li_4Ti_5O_{12}$ (LTO) spinel oxide is currently the most successful material due to its significant reversible capacity of 175 mAh g^{-1} and long cycle life.[12-15] In the present context of exhaustive research on new anodes for safer lithium-ion batteries, other titanium oxide-based materials have been proposed as potential anodes. Several polymorphs of TiO_2 [16,17] and alkali titanates of general formula $A_2Ti_nO_{2n+1}$ (n = 3-9; A = Li, Na, K) with typical operating voltages in the 1.0–2.0 V range are being considered as potential anodes.[18-21] In previous works, the electrochemical and structural characteristics of the $A_2Ti_6O_{13}$ series (A= H, Li and Na) have been investigated.[22-24] The crystal structure of $Na_2Ti_6O_{13}$ is built up of corrugated chains of triple edge-shared TiO_6 octahedra units with approximately rectangular tunnels, in which Na atoms are eightfold coordinated.[25,26] The insertion of up to ca. 3 Li^+ ions has been experimentally demonstrated following two main voltage-composition stages at about 1.35 and 1.12 V vs. Li^+/Li as determined from cyclic voltammetry, delivering 150 mAh g^{-1}. [19,20] Figure 1 shows a typical electrochemical galvanostatic voltage-composition curve for $Na_2Ti_6O_{13}$ vs. Li^+/Li.

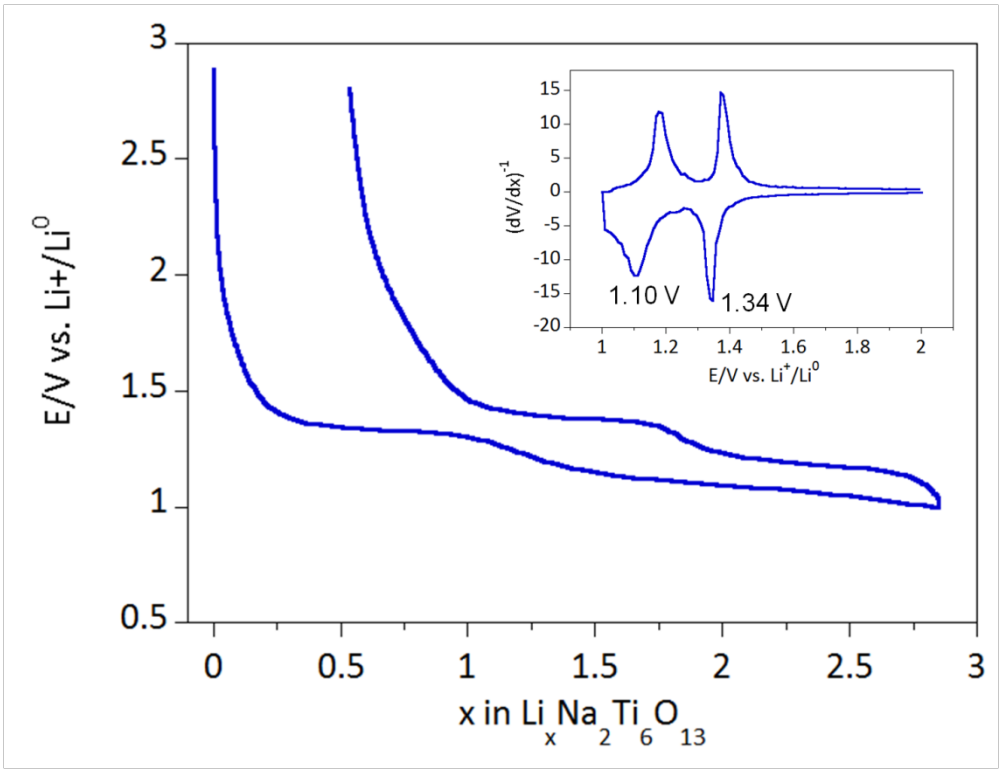

Figure 1. Electrochemical galvanostatic cycling of a $Na_2Ti_6O_{13}$//Li battery at C/10 rate per inserted Li^+ ion. Inset: Incremental capacity curve $(dV/dx)^{-1}$ showing the presence of two main electrochemical features.

The incremental capacity curve (inset) shows two reversible peaks at 1.34 and 1.10 V vs. Li^+/Li for the higher and lower insertion stage, respectively. It has been suggested that a certain irreversible capacity occurring during the low potential stage of lithium insertion is responsible for a lower reversible capacity upon cycling with ca. 2 reversible Li^+ ions. [19] Y. Wang et al. [27] recently reported theoretical calculations predicting intercalation potentials of 1.20 V and 0.89 V. Dominko et al.[19] suggested that lithium insertion in $Na_2Ti_6O_{13}$ occurs in three domains in the 1.5-1.0 V range including two solid solutions up to x = 1, ending up with a biphasic transition for x > 1. In that work evolution of lattice parameters in the solid solution range up to the lithium composition x = 1 was presented; however the phase for x > 1 has not been identified so far. Li et

al.[28] supposed instead a single phase reaction (solid solution) throughout the entire lithium insertion reaction in the 3.0-0.0 V range. However, precise structural information may be missed in Li's study because of the fast cycling rates used during their *in situ* XRD measurements (discharge in 5 hours, with an estimated poor $t_{discharge}/t_{data}$ collection ratio = 10). On the other hand, the structures of lithiated $Na_2Ti_6O_{13}$ compounds have not been solved to date.

For the reasons described above, we aimed at studying the insertion of lithium into $Na_2Ti_6O_{13}$ in a lithium battery during operation (operando) using synchrotron X-ray diffraction. Careful analysis of diffraction data enabled us to follow in detail the structural evolution during lithium insertion in $Na_2Ti_6O_{13}$. Furthermore, high resolution neutron diffraction was used to solve the structures of lithiated $Na_2Ti_6O_{13}$ compounds. Finally, location and mobility of Li^+ and Na^+ ions was investigated by means of neutron Fourier map differences and solid-state ^7Li and ^{23}Na MAS-NMR spectroscopy.

2. Experimental Section

Microcrystalline $Na_2Ti_6O_{13}$ was prepared following the modified sol-gel method previously reported.[29] A 1:1 solution of $Ti(C_4H_9O)_4$ (ρ=0.881 g/mL, ≥97.0%, Aldrich) in 1-butanol (ρ=0.81 g/mL, 99.5%, Scharlau) was dropwise added to the stoichiometric amount of a 1M NaOH aqueous solution under continuous stirring. The resulting solution was heated at 100ºC until a suspension was obtained and finally freeze-dried (0.005 mbar and –49ºC for 48 h). The as-obtained powder was ground and heated at 925ºC for 36 h in air.

$Li_xNa_2Ti_6O_{13}$ samples suitable for neutron powder diffraction were prepared by chemical lithiation of the $Na_2Ti_6O_{13}$ powder with n-butyllithium (1.6 M in hexane, Aldrich). The $Na_2Ti_6O_{13}$ powder (3-4 g) was first mixed with freshly distilled hexane,

and n-butyllithium was slowly added while stirring the mixture. Two $Li_xNa_2Ti_6O_{13}$ samples with nominal compositions x = 1.0 and 2.0 were intended using the corresponding stoichiometric amounts of n-butyllithium. After the reaction mixtures were stirred for 3 weeks at room temperature, samples were filtered, washed repeatedly with hexane and finally dried. All sample preparations were carried out in an argon-filled glovebox to prevent reaction of the lithiated compounds with air and moisture. The effectiveness of chemical lithiation is illustrated by a progressive color change from greyish-blue to dark blue-black. Metals contents of the two lithiated samples were checked by Inductive Coupled Plasma (ICP-OES) spectrometry (Perkin Elmer 3300 instrument) and seen to be x = 0.8 and x = 1.7, lower than those from nominal compositions.

Positive electrodes were prepared by mixing $Na_2Ti_6O_{13}$ with conductive carbon black (Super C65, Imerys, Timcal) and Kynarflex (Elf Atochem) binder in a 65:30:5 weight ratio and pressing the mixture into 8 mm diameter pellets, followed by drying overnight at 80ºC. The active part of the cell was composed of positive electrode, glass fibre separator (Whatman) soaked with 1 M $LiPF_6$ in ethylene carbonate and dimethyl carbonate (1:1 Vol%) as electrolyte and Li metal as negative electrode, assembled in CR2032-type coin cells. Galvanostatic discharge-charge experiments were run at C/10 rate per inserted Li^+ ion using a MacPile II (Biologic Co. Claix, France) potentiostat/galvanostat. For in situ measurements the active stack is inserted between two circular thin aluminum foils (50 μm), which were used for both electrodes as current collector widely transparent to high intensity synchrotron X-rays. We decided in favor of aluminum avoiding completely the use of highly toxic beryllium. Here both the negative and positive casings and the stainless steel spacer disk of the coin cell were provided with circular centred holes (3 mm and 5 mm, respectively) previous to the

assembly of the electrochemical cell inside an Ar-filled glove box. Further details regarding coin cell construction and beamline setup can be found in ref. [30]. The electrochemical galvanostatic experiment was controlled with a MPG-2 multichannel galvanostat-potentiostat. The $Na_2Ti_6O_{13}$//Li cell was discharged to a cut-off voltage of 1.0 V vs. Li^+/Li with a current density of 3.0 mA/g (corresponding to a C/17 rate). At mid charge state, charge was completed with a higher current density of 5.0 mA/g (C/10 rate) to the end of charge of the cell. This configuration ensured synchrotron X-ray data of a complete discharge-charge cycle were collected. Compared to $Na_2Ti_6O_{13}$//Li cells discharged in conventional *ex situ* coin cells, no significant changes of voltage, shape of discharge-charge curves or capacities were observed indicating that the data collected under this in situ regimen represents the electrochemical behavior of $Na_2Ti_6O_{13}$ electrodes in conventional lithium half cells.

Operando synchrotron XRD experiments were performed on the beamline BM20 at the Helmholtz-Zentrum Dresden-Rossendorf at ESRF (Grenoble, France) Transmissions geometry was chosen, going the beam through all the layers of the in situ cell. The wavelength was 0.49000(5) Å throughout the whole experiment, selected by means of a double-crystal Si(111) monochromator. XRD data were collected continuously in the range 2-36º in 7 minute acquisitions throughout a complete charge-discharge cycle. The experimental ratio full discharge time/acquisition time > 300 ($t_{discharge}/t_{data}$ collection= 2322 min/7 min = 332) guaranteed that highly reliable data with negligible Δx for each diffraction pattern were collected throughout all electrochemical measurements. As the beam is going through all layers in the battery, additional Bragg peaks from lithium and aluminum (two windows between which the active cell is placed) are generated. The 2θ regions where these peaks occur can be eliminated by comparing the whole pattern obtained in the in situ cell with the pure pristine phase. Figure S1 (Supplemental

Information) shows the full measured 2θ range, in which the positions of the extra Bragg peaks are marked. The absorption of the sample is taken into account using the correction factor for flat-plate samples in transmission geometry. For a correct refinement of data, we followed a protocol similar to the one given by M. Bianchini et al.[31]. At first zero-shift was determined using the pristine $Na_2Ti_6O_{13}$ with well-known unit cell parameters. Secondly, this zero-shift parameter was used and fixed throughout all subsequent refinements. In table S1 (Supplemental Information) results of refinements of pristine $Na_2Ti_6O_{13}$ from data collected in capillary and those available from previous reports are compared with actual results using the in situ cell. All data treatments were performed using the Fullprof program.[32]

High resolution neutron powder diffraction (NPD) was performed at SPODI (Heinz Maier-Leibnitz source FRM II, Garching, Germany). All sample compositions x = 0, 0.8 and 1.7) were measured at 300 K in the range 3-150º using the wavelength 1.5484 Å selected with a Ge(551) monochromator. Samples were loaded in argon atmosphere in airtight vanadium cans sealed with indium O-rings to prevent them from reaction with moisture and air. Rietveld refinement[33,34] was performed using the Fullprof program.[32] The negative neutron scattering length factor of Li increases considerably the contrast with respect to light Na and O atoms, enabling Fourier density map investigations addressed to localize Li atoms. Fourier density difference maps were built using the GFourier package incorporated in Fullprof.[32] The coherent neutron scattering lengths used were: Ti: –3.438 fm; Li: –1.90 fm; Na: +3.63 fm and O: +5.80 fm.[35] Bond valence sum maps were calculated utilizing the BVS Mapping package incorporated in Fullprof.[32] Structural models were visualized using the Vesta software.[36]

^{23}Na and ^{7}Li NMR spectra were recorded at room temperature after single pulse (3 μs) irradiation of samples in an Avance-400 Bruker spectrometer working at 105.4, and

155.45 MHz respectively (external magnetic field, 9.4 T). In MAS (magic angle spinning) experiments, the rotor was of Andrew type and the spinning frequency 10 KHz. The recycling delay used in accumulations was 10 s. Signal/noise ratios better than 50 were obtained by increasing the amount of accumulations above 100 and 50, respectively. Filters used on recording central components were 100 kHz, but those used in recording spinning sidebands patterns were between 300 and 2000 kHz. The analysis of NMR spectra was carried out with the Winfit (Bruker) software. From spinning side band patterns, quadrupole constants C_Q and η of different components were estimated by trial and error procedures. From the fitting of experimental envelopes, relative intensities of different components were estimated.

Li insertion produces the reduction of titanium cations, increasing paramagnetic interactions between Li^+ and Ti^{3+} cations. Paramagnetic interactions increase with magnetic field and decreases with temperature. In general, isotropic contact interactions are responsible for detected shifts and dipolar interactions for observed broadening of powder NMR components.[37] In the last case, all possible orientations of crystallites with respect to the external magnetic B_0 increase the paramagnetic broadening of NMR signals. The sample rotation averages paramagnetic interactions; however, the full cancellation was difficult to achieve in MAS experiments. ^{7}Li MAS NMR experiments were performed at increasing temperatures from room temperature to 140° C with steps of 20º C. Before recording NMR spectra, a stabilization of 5 min. was used for all temperatures. To verify the reversibility of the process, the spectrum at room temperature obtained after cooling was also recorded.

3. Results

As described above in Figure 1, a common characteristic of $Na_2Ti_6O_{13}$ is a two-stage lithium insertion process in the 1.0-1.5 V range, exhibiting two voltage regions, a higher one around 1.3 V vs. Li^+/Li and a lower one around 1.1 V vs. Li^+/Li.

In situ evolution of the $Na_2Ti_6O_{13}$ electrode during lithium insertion.

The structural changes of the $Na_2Ti_6O_{13}$ electrode during galvanostatic cycling in the 3.0 - 1.0 V potential range have been investigated by operando synchrotron X-ray diffraction measurements. Figure S2 (Supplemental Information) shows the complete set of synchrotron XRD patterns collected in the 3-19º diffraction range throughout the first discharge - charge cycle as two-dimensional contour diagram. The reversible evolution of Bragg peaks throughout the discharge-charge cycle confirms the reversibility of structural changes. Figure 2 shows the synchrotron XRD patterns collected upon insertion of lithium in $Na_2Ti_6O_{13}$ during the galvanostatic discharge stage. Selected compositions and their corresponding XRD patterns are highlighted with colored spots. These are pristine $Na_2Ti_6O_{13}$ (black) and $Li_{0.8}Na_2Ti_6O_{13}$ (blue); hereafter it is shown that they correspond to the single-phase domain; $Li_{1.6}Na_2Ti_6O_{13}$ (red) and $Li_{2.4}Na_2Ti_6O_{13}$ (green); hereafter it will be shown that they correspond to initial and advanced state of the biphasic domain. A continuous shift of diffraction peaks (labelled P1 in Figure 2) is observed in the range $0<x\leq1.5$, characteristic for a single phase solid solution mechanism. In this compositional range careful analysis of characteristic serial reflections (*h*00), (0*k*0), (00*l*) of the monoclinic cell shows that (002) and (020) reflections (Figures S2 and 2) are continuously shifted to lower diffraction angles during lithium insertion up to x=1.5, in agreement with the increase observed of both *c* and *b* parameters portrayed in Figure 3. On the other hand, (-201) and (-202) reflections (Figure S2) are sensitive probes to variations of the monoclinic β angle, consistent with

a decrease of the β angle (Figure 3). Interestingly, this trend is opposite to that found during insertion of Na in $Na_2Ti_6O_{13}$.[38] Finally notwithstanding the slight continuous shift of the (200) reflection (Figure S2) to lower diffraction angles during lithium insertion, the *a* parameter remains practically unaltered. This is the result of the combined effect of both decreasing d spacings of (*h*00) lattice planes and decreasing monoclinic angle, owing to the mathematical expression for the monoclinic system:

$\cos(90-\beta) = d\{100\}/a$ or $a = d\{100\}/\cos(90-\beta)$ (1)

For compositions x > 1.5 diffraction peaks of the pristine $Na_2Ti_6O_{13}$ or single domain $Li_xNa_2Ti_6O_{13}$ lose intensity, while new one starts growing. This is especially noticeable in Figure 2 for diffraction peaks (labelled P2 in Figure 2) with contribution along the *b* direction, e.g. (110), (310) and (020). The new single phase found here is described in the same monoclinic space group *C*2/*m*, but with modified unit cell parameters as shown in Figure 3, in good agreement with predictions from theoretical calculations.[27] Phase transformation was not completed at the end of discharge of the in situ cell.

Overall from $Na_2Ti_6O_{13}$ to $Li_{2.4}Na_2Ti_6O_{13}$ passing through the single phase $Li_{1.5}Na_2Ti_6O_{13}$, the unit cell volume increases from V = 510.56(2) Å^3 to 535.65(2) Å^3 with an overall variation $\Delta V/V$ = +4.9%, which underlies significant anisotropy in cell parameter variations: $\Delta a/a$ = -0.3%, $\Delta b/b$ = +3.2%, $\Delta c/c$ = +1.6%, $\Delta\beta/\beta$ = -2.6%. Interestingly, the corresponding variations are rather small within the solid solution domain with a unit cell volume variation $\Delta V/V$ = +1.6%, in which anisotropy is much less accentuated ($\Delta a/a$ = -0.09%, $\Delta b/b$ = +0.58%, $\Delta c/c$ = +0.8%, $\Delta\beta/\beta$ = -0.3%). This observation may explain why excellent cyclability occurs in the solid solution domain, but capacity fades significantly when cells are cycled in the whole insertion range [19] because of a more pronounced stress of the material. It is worth mentioning that cell parameters of both phases continue to vary in the biphasic domain $Li_{1.5}Na_2Ti_6O_{13}$ -

$Li_{2.4}Na_2Ti_6O_{13}$, in contrast to the expected behavior (two phases are expected to change in relative weight throughout the biphasic region with constant amount of lithium in every phase and hence constant cell parameters). This is well inferred from Figure 2 where the (020) diffraction peak of both phases inversely changes intensity but also shifts at the same time. This anomalous behavior has been recently described for other materials as related to particle size, strain or high-rate (non-equilibrium) cycling.[39-41]

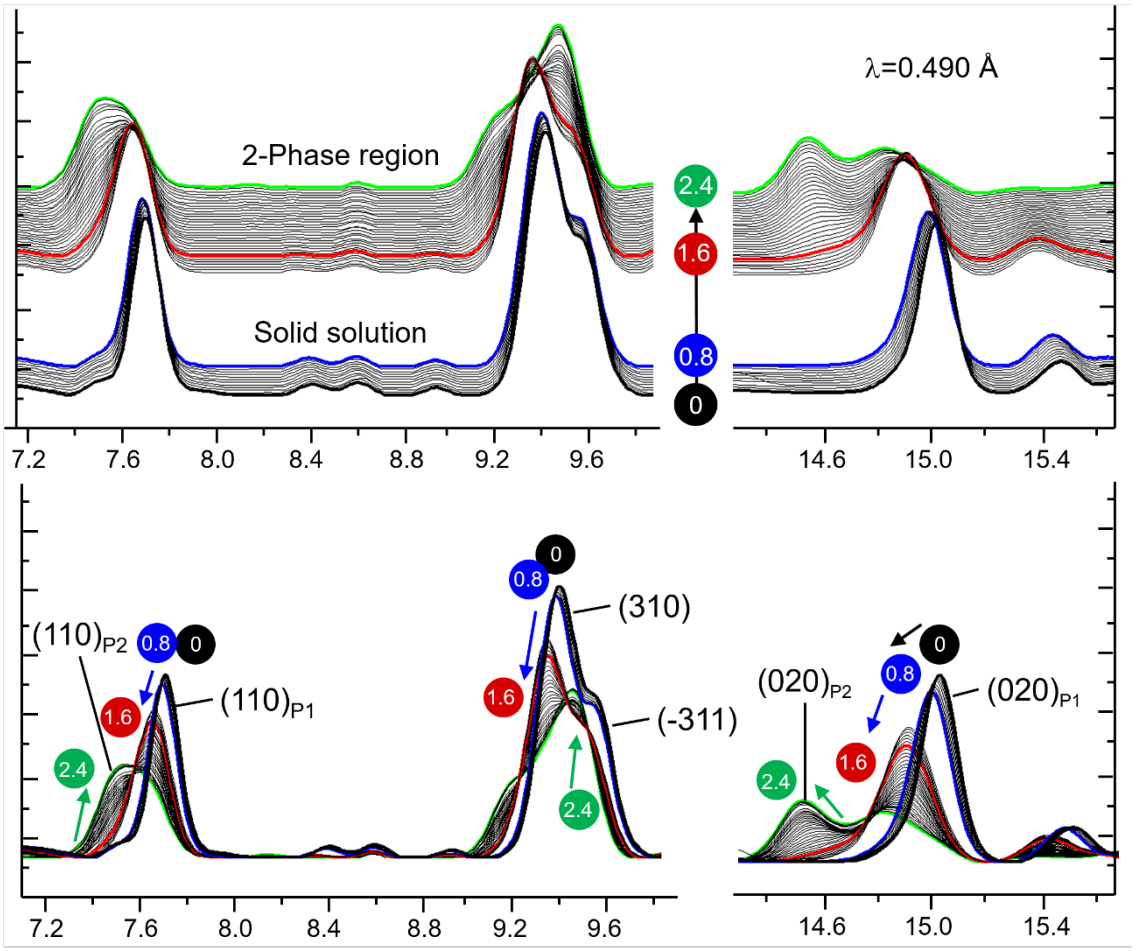

Figure 2. Selected angular regions during insertion of lithium in $Na_2Ti_6O_{13}$. Single phase domain covers x=0 (black) to x=1.5. The intermediate x=0.8 is highlighted (blue). Beginning of biphasic domain from x=1.6 (red) until end of discharge (x=2.4, green) are shown. 7.1-9.9º (left) and 14.3-15.7º (right).

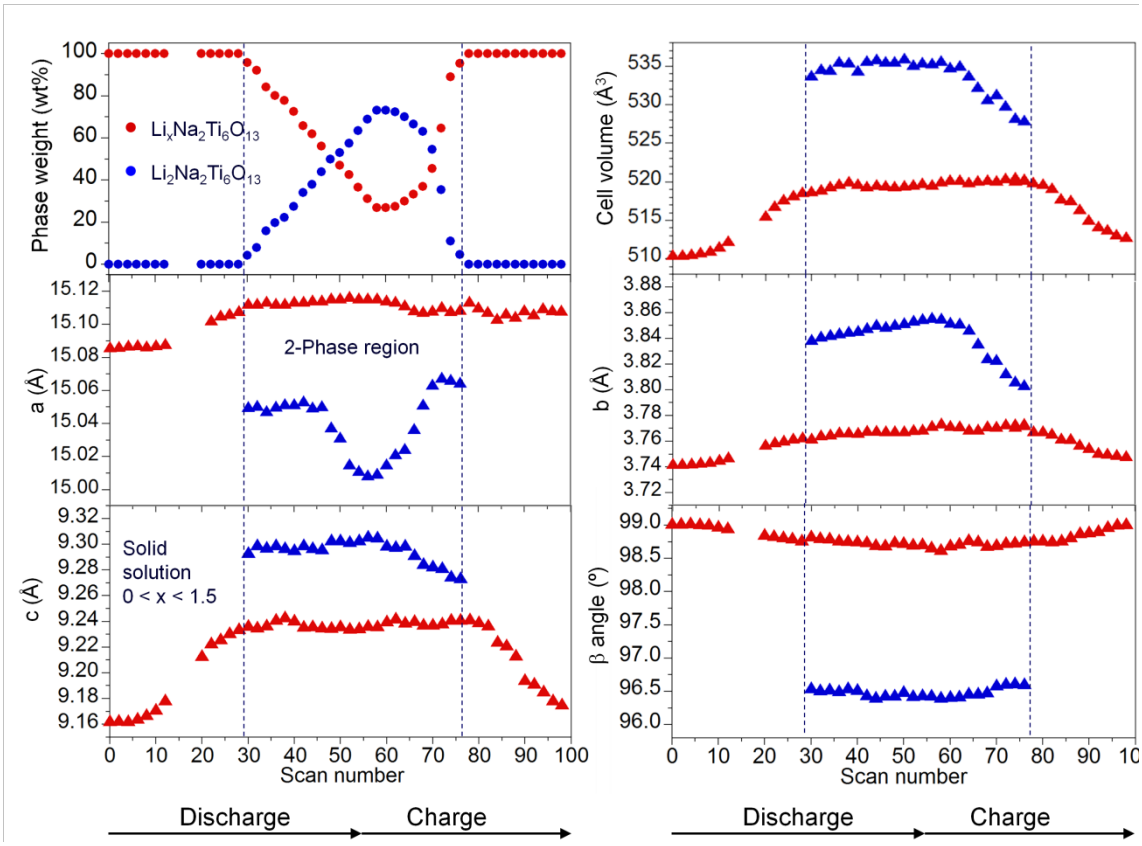

Figure 3. Unit cell parameters of the two monoclinic phases and relative percentage in weight are presented. Both phases are described in the space group *C*2/*m*.

Finally, the phase diagram found and analyzed in this study is given in Figure 4. The variation of charge Q as a function of √t obtained by using the potentiostatic intermittent titration technique (PITT) has been included. It is seen that Q exhibits a linear variation with √t in the high voltage insertion stage (1.35 V), characteristic of the solid solution domain, whereas it clearly deviates from linearity in the low voltage insertion stage (1.10 V), in full agreement with our operando synchrotron XRD study.

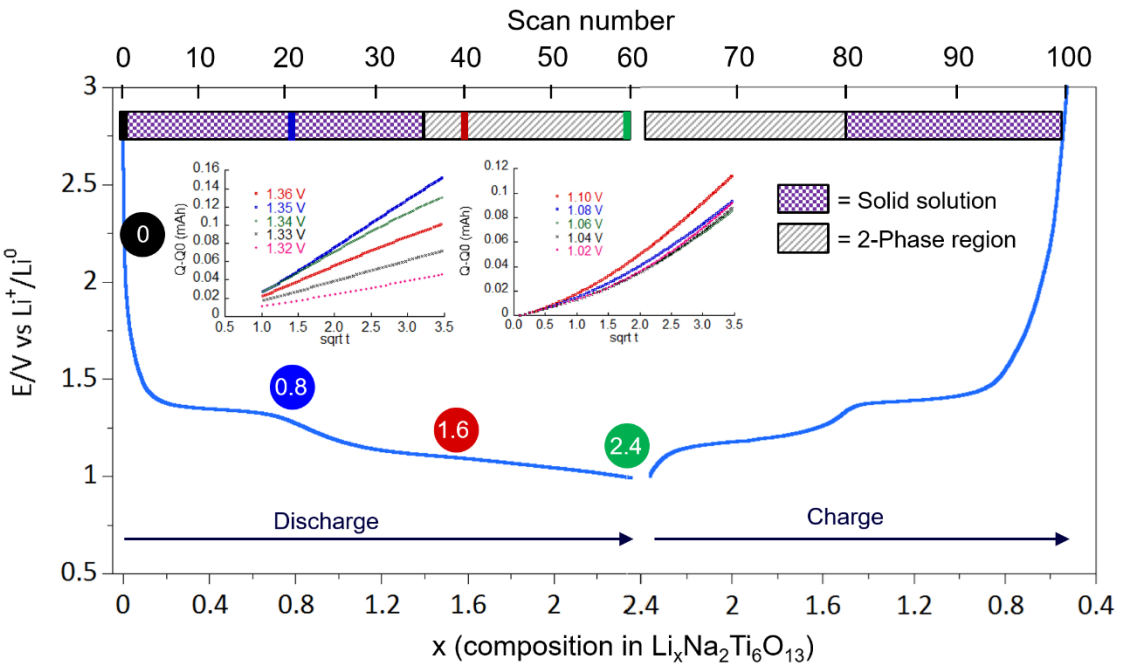

Figure 4: Voltage-composition curve obtained during lithium insertion in $Na_2Ti_6O_{13}$. The (galvanostatic) discharge stage was completed while recording 58 7 min. diffraction scans, whereas the charge was performed while recording 39 7 min. diffraction scans. The horizontal bar (top of figure) shows the nature of the observed insertion mechanism and selected compositions are highlighted with colored spots. Solid solution: initial state (black), intermediate state (blue). Beginning two-phase region (red). End of discharge (green). The variation of charge Q as a function of √t for both high and low voltage insertion stages are inset.

Crystal structures of lithiated compounds $Li_{0.8}Na_2Ti_6O_{13}$ and $Li_{1.7}Na_2Ti_6O_{13}$. To assess the Li distribution in $Li_xNa_2Ti_6O_{13}$, two chemically lithiated compositions, x = 0.8 and 1.7 which correspond to intermediate and nearly end compositions of the solid solution, were investigated by means of high resolution neutron diffraction. It is worth noting that the upper Li compositional limit deduced from the in situ XRD study performed under non-equilibrium cycling conditions (previous section) was slightly

lower, x=1.5. Preparation of the second phase with higher lithium content (x > 1.7) after the biphasic region deduced from in situ XRD measurements was not possible, most likely owing to the lower reduction potential needed for forming that phase (about 1 V vs. Li^+/Li). The crystal data and refinement parameters of $Li_{0.8}Na_2Ti_6O_{13}$ and $Li_{1.7}Na_2Ti_6O_{13}$ are given in Table 1.

Table 1. Crystal data and refinement parameters for $Li_{0.8}Na_2Ti_6O_{13}$ and $Li_{1.7}Na_2Ti_6O_{13}$ obtained from neutron diffraction. Starting $Na_2Ti_6O_{13}$ is included for comparison.

Compound	$Na_2Ti_6O_{13}$ (from [24])	$Li_{0.8}Na_2Ti_6O_{13}$	$Li_{1.7}Na_2Ti_6O_{13}$
Space group	*C*2/*m* (#14)	*C*2/*m* (#14)	*C*2/*m* (#14)
a (Å)	15.1032(2)	15.0905(4)	15.1019(7)
b (Å)	3.7437 (1)	3.7470(1)	3.7679(2)
c (Å)	9.1713(2)	9.1780(2)	9.2520(5)
β (º)	99.056(1)	98.992(2)	98.813(4)
Volume ($Å^3$)	512.10(1)	512.59(2)	520.25(4)
R_{exp} (%)	1.45	1.74	1.78
R_{wp} (%)	3.36	3.18	3.90
R_p (%)	2.64	2.51	2.92
χ^2	5.38	3.35	4.79
R_F (%)	2.22	2.85	1.31
R_{Bragg} (%)	2.85	4.56	2.15

As a general consideration, changes in lattice parameters are small, suggesting easy lithium insertion in line with electrochemical lithium insertion reported for $Na_2Ti_6O_{13}$.[19] The moderate changes produced in unit cell parameters of $Na_2Ti_6O_{13}$ during lithium insertion (as determined by operando synchrotron X-ray diffraction) support the hypothesis that only minor structural modifications occurred in $Na_2Ti_6O_{13}$ during lithiation. Starting atomic positions for sodium, titanium and oxygen given for $Na_2Ti_6O_{13}$ [24] were used for Rietveld refinements. The corresponding difference Fourier synthesis maps were calculated using the $Na_2Ti_6O_{13}$ structure (Figure 5a), in which Li atoms were not included for x=0.8 (Figure 5b) and x=1.7 phases (Fig. 5c and d).

For $Li_{0.8}Na_2Ti_6O_{13}$ (Figure 5b) a single negative peak for Li in the *y*/*b* = 0.5 section was detected at 2*c* (½, ½, ½) channel sites (labelled Li1). For the sake of completeness Li sites were validated by probing the simulated annealing technique implemented in Fullprof.[42] After lithium was initially placed on a general xyz site, the convergence was reached at x=0.48, y=0.48 and z=0.52, near 2*c* positions. Interestingly $Li_{1.7}Na_2Ti_6O_{13}$ (Figure 5c) displays two additional negative peaks for Li at 4*i* channel sites in the y/b = 0.5 section, at coordinates x ~ 0.46 and z ~ 0.14 (labelled Li2), and in the y/b = 0 section, at coordinates x ~ 0.56 and z ~ 0.47 (labelled Li3). The observed negative peaks Li1 and Li2 match with those predicted on the basis of geometric considerations.[24]

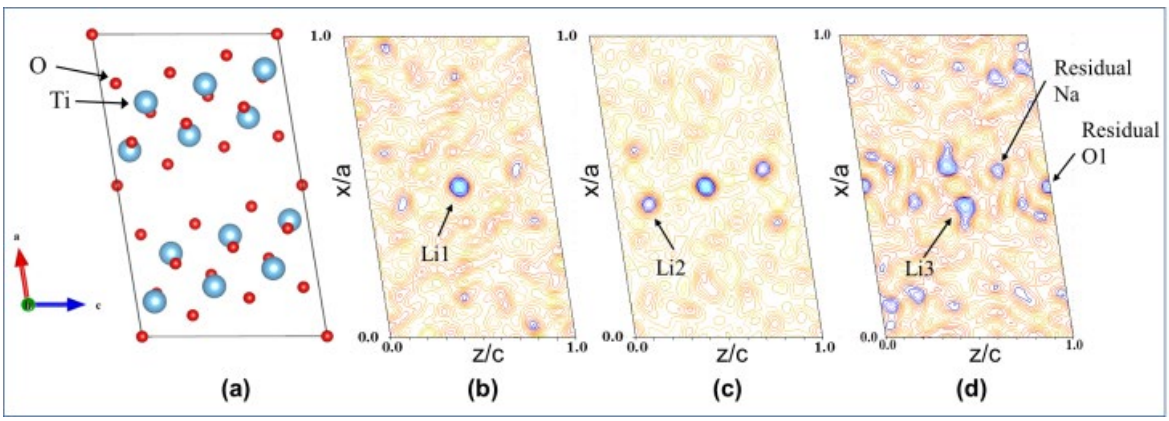

Figure 5. The $Na_2Ti_6O_{13}$ framework with the unit cell shown in black (a). Two-dimensional difference Fourier synthesis maps from NPD patterns at the y/b = 0.5 section of $Li_{0.8}Na_2Ti_6O_{13}$ (b) and $Li_{1.7}Na_2Ti_6O_{13}$ at y/b = 0.5 (c) and y/b = 0.0 (d). The negative residual nuclear scattering length density at 2*c* and 4*i* channel sites corresponds to Li atoms.

In Rietveld refinement models without lithium, only fractional atomic coordinates of Na, Ti and O atoms were allowed to vary, yielding reliability factors: R_p = 5.51%, R_{wp} = 7.19%, χ^2 = 16.3, R_B = 23.6%, R_F = 16.5% ($Li_{0.8}Na_2Ti_6O_{13}$) and R_p = 4.82%, R_{wp} = 6.12%, χ^2 = 11.8, R_B = 13.6%, R_F = 9.30% ($Li_{1.7}Na_2Ti_6O_{13}$). For $Li_{0.8}Na_2Ti_6O_{13}$ a single lithium Li1 was introduced at special 2*c* positions (½, ½, ½) and the site occupancy factor (SOF) was fixed at 1.0. For $Li_{1.7}Na_2Ti_6O_{13}$ additional lithium Li2 and Li3 were placed at 4*i* sites with SOF initially fixed at 0.5. The site occupancy (SOF) of the Li positions was refined with fixed atomic coordinates and isotropic thermal U_{iso} factors. In general it was not possible to refine simultaneously the SOF, xyz coordinates and U_{iso} for Li. Reliability factors of final refinements are shown in Table 1 and the graphical results summarized in Figure 6.

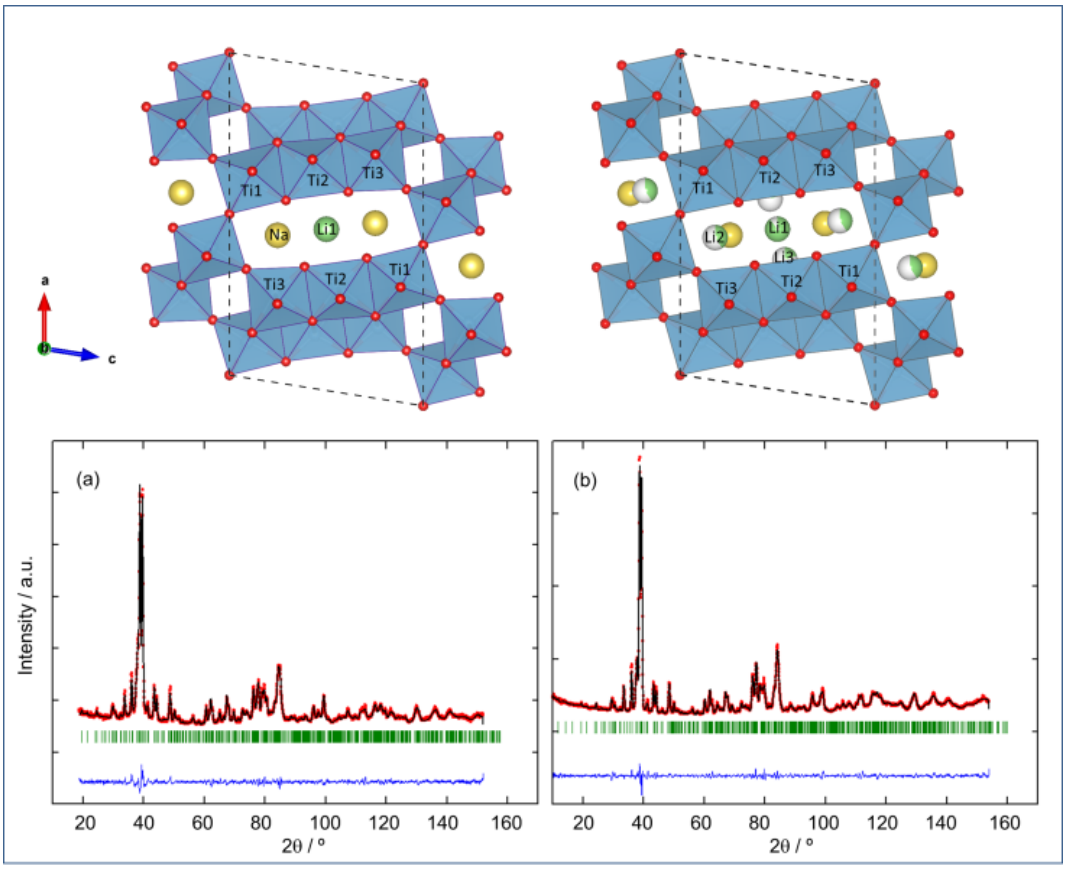

Figure 6. Rietveld refinement plot for neutron diffraction data and the respective structural model of $Li_{0.8}Na_2Ti_6O_{13}$ (a) and $Li_{1.7}Na_2Ti_6O_{13}$ (b), with observed (points), calculated (solid line) profiles, and difference on the same scale. The positions of reflections are marked by vertical bars.

The comparative analysis of $Na_2Ti_6O_{13}$, $Li_{0.8}Na_2Ti_6O_{13}$ and $Li_{1.7}Na_2Ti_6O_{13}$ shows that the basic framework structure is formed by zigzag chains of triple edge-shared TiO_6 octahedra, sharing corners between neighboring structural units. This arrangement of octahedra favors creation of conduction channels along the *b*-axis, alternating structural blocks and conduction paths disposed along *a* and *c* axis. The structural network, in which Na and Li ions are allocated at different sites, can be considered extremely rigid, and structural changes are limited to slight changes in Ti and O positions, Ti-O distances and Ti-O-Ti angles. To better analyze structural features of these compounds, Rietveld

analysis of neutron diffraction patterns was performed. In this analysis Li sites and site occupancies were deduced. Finally, Li mobility was investigated by comparing thermal B factors deduced from ND and narrowing of NMR components deduced during heating of samples. The study of ^{7}Li and ^{23}Na MAS-NMR signals permits the nature of charge carriers to be deduced.

Structure of $Li_{0.8}Na_2Ti_6O_{13}$. The atomic coordinates and thermal parameters of $Li_{0.8}Na_2Ti_6O_{13}$ are given in Table 2, and selected interatomic distances are listed in Table S2. The Li SOF for 2*c* sites refined to 0.90(3), in good agreement with chemical analysis. The $Li_{0.8}Na_2Ti_6O_{13}$ structure, illustrated in Figure S3a, is similar to $Na_2Ti_6O_{13}$. The $Ti_6O_{13}^{2-}$ framework built from distorted TiO_6 octahedra exhibits Ti-O distances in a wide range from 1.789(6) (Ti1) to 2.255(7) Å (Ti2). The most remarkable characteristic of the $Li_{0.8}Na_2Ti_6O_{13}$ structure is the LiO_4 planar coordination adopted by lithium, slightly distorted with Li-O distances ranging from 2.038(2) to 2.335(2) Å. This coordination is unusual for Li atoms in oxides, but was found in the closely related $Li_2Ti_6O_{13}$.[22,43] LiO_4 tetrahedral or LiO_6 octahedral are not possible in the tunnel space of $Na_2Ti_6O_{13}$, where the shortest Li-Na and Li-Ti (between Li1 and Ti2) distances are 2.966(3) and 2.694(2) Å (see also Table S3 of Supplemental Information). The calculated bond valence sum for Li sites was 0.62+, suggesting some disordering around 2*c* positions. Indeed the result from the simulated annealing technique used to locate lithium may hint at a disorder displacement of lithium from 2*c* sites. In this compound Na ions are clearly underbonded, 0.63+ compared to the formal valence state (1+), like in $Na_2Ti_6O_{13}$.[24,43]

Table 2. Fractional atomic coordinates, site occupancy factors (SOF) and isotropic thermal parameters U_{iso} for $Li_{0.8}Na_2Ti_6O_{13}$; space group *C*2/*m*

Atom	Site	x/a	y/b	z/c	SOF	$U_{iso}x10^2$ (Å^2)
Na1	4*i*	0.4566(3)	0	0.2484(5)	1	1.33(3)
Ti1	4*i*	0.1133(3)	0	0.0955(5)	1	0.46(1)
Ti2	4*i*	0.1682(3)	0	0.4393(6)	1	0.46(1)
Ti3	4*i*	0.2223(3)	0	0.7663(5)	1	0.46(1)
O1	2*c*	0	0	0	0.5	0.48(1)
O2	4*i*	0.2442(2)	0	0.2472(3)	1	0.48(1)
O3	4*i*	0.0704(2)	0	0.2912(3)	1	0.48(1)
O4	4*i*	0.2910(2)	0	0.5715(3)	1	0.48(1)
O5	4*i*	0.1269(2)	0	0.6118(3)	1	0.48(1)
O6	4*i*	0.3574(2)	0	0.8817(3)	1	0.48(1)
O7	4*i*	0.1625(2)	0	0.9131(3)	1	0.48(1)
Li1	2*c*	0.5	0.5	0.5	0.80(3)	1.6

Structure of $Li_{1.7}Na_2Ti_6O_{13}$. The atomic coordinates and thermal parameters of $Li_{1.7}Na_2Ti_6O_{13}$ are summarized in Table 3 and selected interatomic distances provided in Table S4 (Supplemental Information). The refined Li1 SOF at 2*c* site was 0.88(1), while Li2 and Li3 ones (both at 4*i* sites) were 0.41(1) and 0.15(1), consistent with the chemical composition. The framework structure of $Li_{1.7}Na_2Ti_6O_{13}$ in Figure S3b is similar to that of $Li_{0.8}Na_2Ti_6O_{13}$. When going from $Li_{0.8}Na_2Ti_6O_{13}$ to $Li_{1.7}Na_2Ti_6O_{13}$, Ti and Li polyhedra become more symmetrical. The range of Ti-O distances becomes narrower being now comprised between 1.848(6) (Ti1) and 2.148(7) Å (Ti3).

Table 3. Fractional atomic coordinates, site occupancy factors (SOF) and isotropic thermal parameters U_{iso} for $Li_2Na_2Ti_6O_{13}$; space group *C*2/*m*

Atom	Site	*x/a*	*y/b*	*z/c*	SOF	U_{iso}x10^2 (Å^2)
Na1	4*i*	0.4571(3)	0	0.2419(4)	1	1.60(2)
Ti1	4*i*	0.1141(3)	0	0.1020(5)	1	0.62(1)
Ti2	4*i*	0.1698(3)	0	0.4258(6)	1	0.62(1)
Ti3	4*i*	0.2274(2)	0	0.7617(4)	1	0.62(1)
O1	2*c*	0	0	0	0.5	0.58(1)
O2	4*i*	0.2412(2)	0	0.2523(3)	1	0.58(1)
O3	4*i*	0.0653(2)	0	0.2997(3)	1	0.58(1)
O4	4*i*	0.2930(2)	0	0.5714(3)	1	0.58(1)
O5	4*i*	0.1234(2)	0	0.6142(3)	1	0.58(1)
O6	4*i*	0.3578(2)	0	0.8809(3)	1	0.58(1)
O7	4*i*	0.1708(2)	0	0.9099(3)	1	0.58(1)
Li1	2*c*	0.5	0.5	0.5	0.82(2)	5.0(2)
Li2	4*i*	0.445(1)	0.5	0.171(1)	0.31(1)	1.1(2)
Li3	4*i*	0.591(2)	0	0.462(3)	0.13(1)	2.8(4)

The bond valence sums for the three Ti sites in $Na_2Ti_6O_{13}$ were +4.205 for Ti1, +4.124 for Ti2 and +4.154 for Ti3, consistent with the formal valence of +4 for all Ti atoms (see also Table S5). For lithiated $Li_{1.7}Na_2Ti_6O_{13}$ bond valence sums were +3.747 for Ti1 sites, +3.928 for Ti2 sites and +4.289 for Ti3 sites. These results suggest the location of Ti^{4+} at central Ti2 and Ti^{3+} cations at external Ti1 sites. The decrease of the oxidation state of Ti decreases Ti-Ti repulsions. Interestingly, Li2 atoms adopt strongly

distorted LiO_4 square planar coordinations in $Li_{1.7}Na_2Ti_6O_{13}$, with Li-O distances ranging from 1.834(2) to 2.277(2) Å. The Li2 site found in $Li_{1.7}Na_2Ti_6O_{13}$ is nearly identical to Li positions reported in $Li_2Ti_6O_{13}$.[22,24,40] The Li3 adopts a LiO_5 square pyramidal coordination, with Li-O distances ranging from 1.718(2) to 2.402(2) Å. Li *et al.* indicated that additional intercalating lithium would likely reside in this fivefold coordinated site (4*i*), shifted from the center of the tunnel, or in the central site (2*d*) between the two sodium atoms.[28] We probed placing Li in 2*d* (½, 0, ½), however structural refinements were not stable. This result was expected, inasmuch as lithium placed in the central tunnel site would produce inappropriate Li coordination, exhibiting a square prismatic LiO_8 coordination with large Li-O distances (2.75-2.98 Å) and short Li-Na distances of 2.24 Å. The calculated bond valence sums for the Li sites were 0.71+ for Li1, 0.97+ for Li2 and +0.84 for Li3. Table S3 (Supplemental Information) shows that the Li1-Ti2 distance is 2.754(5) Å compared to 2.694(6) Å in $Li_{0.8}Na_2Ti_6O_{13}$, with the shortest Li-Ti distance (between Li3 and Ti2) being 2.280(9) Å. While Li1-Na and Li1-Li2 distances remain at large 2.931(3) and 2.952(2) Å, partially occupied Li2 sites exhibit significantly shorter distances of 2.012(2) Å to Na.

MAS-NMR spectroscopy

^{23}Na MAS-NMR spectra. In ^{23}Na (I=3/2) MAS-NMR spectra central (1/2,-1/2) and satellite (3/2,1/2) and (3/2,1/2) transitions are modulated by spinning side bands (ssb) produced by the sample rotation (spinning rate, 10 kHz); however, in $Na_2Ti_6O_{13}$ satellite transitions were hardly detected because of polyhedra distortions and cation disorder (Figure 7a). In our samples, differences on quadrupolar interactions enlarge side bands beyond its detection, impeding the analysis of first order quadrupolar patterns. A deeper analysis of the central transition shows the presence of several resolved maxima

separated by hard discontinuities that are associated with well-defined electric field gradient components at Na sites. The simulation of experimental profiles with second order quadrupolar interactions showed that the experimental profile can be reproduced with C_Q = 2.7 MHz and η = 0.7 quadrupolar constants. Important deduced values are due to the shift of Na ions from polyhedra centers. The chemical shift deduced after correction of quadrupolar shift effects, -12.2 ppm, agrees with the eightfold coordination deduced by neutron diffraction analyses. In deconvolution of spectra the intrinsic linewidth used in spectral fitting was small (Em ~ 5), indicating in agreement with ND patterns that the chemical environments of Na are well defined.

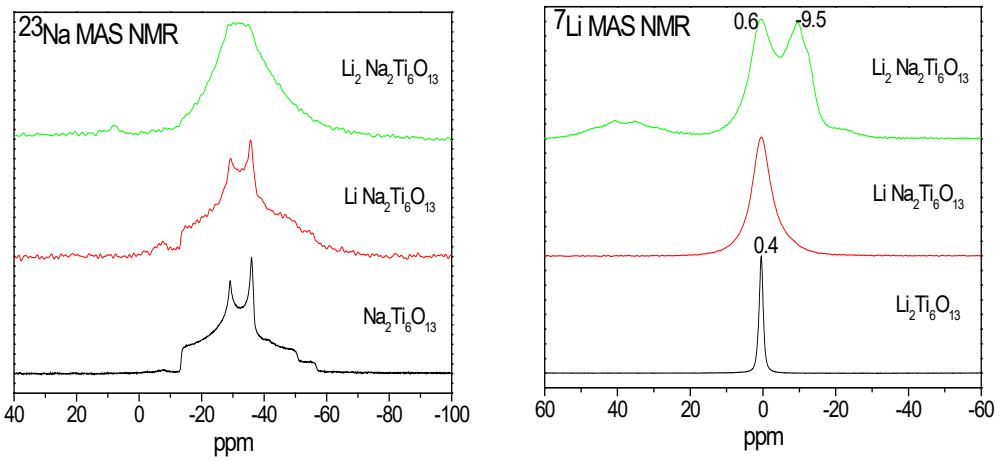

Figure 7. a) The central transition of the ^{23}Na MAS-NMR spectrum of $Na_2Ti_6O_{13}$ and the lithiated phases recorded at 9.4 T; b) The central transition of ^{7}Li MAS-NMR spectra of lithiated $Na_2Ti_6O_{13}$ phases. The Li exchanged $Li_2Ti_6O_{13}$ compound has been included for comparison.

In $Li_{0.8}Na_2Ti_6O_{13}$ (Figure 7a) some loss on definition of second order quadrupolar interactions in the sodium central component of spectra was produced, suggesting the presence of some paramagnetic broadening. The ^{23}Na MAS NMR spectrum of

$Li_{1.7}Na_2Ti_6O_{13}$ in Figure 7a shows an additional broadening that precludes the identification of quadrupolar patterns.

^{7}Li MAS-NMR spectra. In ^{7}Li (I=3/2) MAS-NMR spectrum, sidebands patterns of inserted Li are better defined than in sodium spectra. To improve experimental resolution, ^{7}Li MAS-NMR spectra of three samples were recorded (Figure 7b). In this case, the central (1/2,-1/2) transition was formed by a single component and satellite (3/2,1/2) and (-3/2,-1/2) transitions formed by a big number of spinning side bands that cover a larger region (Figure S4, Supplemental Information). The experimental ^{7}Li MAS-NMR spectra of the Li exchanged sample, $Li_{1.7}Ti_6O_{13}$, was included for sake of comparison.

The spectrum of $Li_{0.8}Na_2Ti_6O_{13}$ in Figure 7b shows a single component at 0.36 ppm, with a 6.64 ppm linewidth. Quadrupolar C_Q constant and asymmetric η constants were 108 kHz and 0.7 (Figure S4a). As lithium insertion progresses the spectrum changes dramatically, remaining the signal observed at 0.39 ppm for $Li_{0.8}Na_2Ti_6O_{13}$ and appearing two new components at -9.5 and 38.3 ppm, which are shifted by paramagnetic interactions (Figure 7). The analysis of ssb patterns was difficult due the simultaneous presence of quadrupolar and paramagnetic contributions. In the case of Na cations, chemical shift values are not affected by interaction with Ti^{3+} cations (Na-Ti distance > 4.5 Å). The use of high magnetic fields enhances paramagnetic interactions, favoring the differentiation of lithium ions bonded to octahedral Ti^{3+} and Ti^{4+} cations. Taken into account BVS results (Table S4) deduced in refinements, the location of Ti^{4+} at central Ti2 and Ti^{3+} cations at external Ti1 sites seems to be produced. From this fact, paramagnetic interactions on external Li2 sites, sharing oxygen atoms with Ti^{3+} cations, will be higher than in Li1 sites, where oxygen is bonded to Ti^{4+} cations.

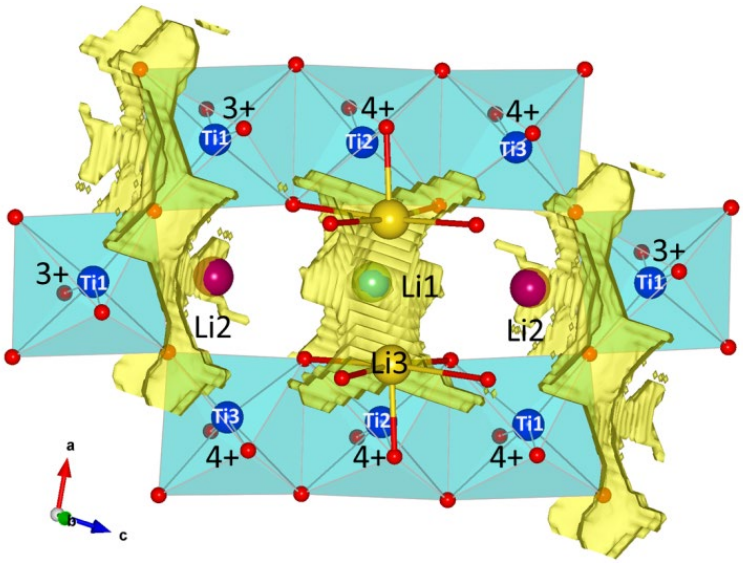

Figure 8. Crystal structure of $Li_{1.7}Na_2Ti_6O_{13}$ viewed along the [010] direction. Green and red spheres denote central Li1 and external Li2 at y/b = 0.5. Li3 in square pyramidal coordination located at the y/b = 0 section is depicted as yellow sphere. Possible diffusion pathway of mobile lithium ions as deduced from BVS isosurfaces (yellow) is overlaid on the structure.

In Li-O-Ti^{3+} associations, Ti^{3+} cations modify the charge of oxygen atoms, affecting the electron density in 1s orbitals of lithium. This makes isotropic chemical shift values of lithium to change, improving Li species resolution. In shifted components, a dipolar paramagnetic broadening enlarges components, reducing experimental resolution of two Li2 sites at -9.5 and -11 ppm. An analysis of Li environments shows that Li2 ions can be subjected to 1 or 2 Ti^{3+} paramagnetic interactions. Based on Ti-Li distances we have assigned two detected components to these two environments in Figure 8. Different coordination of lithium affects electron density at 1s Li orbitals. The assignment of the ~+40 ppm signal is more difficult because of its positive chemical shift value. To understand different charge density associated with Li3 ions, we have analyzed other Li sites detected by Fourier map differences. In particular, five-fold LiO_5 coordinated sites

allocated at the planes occupied by sodium (y/b = 0) could display different features (Figure 8). The assignment of three Li NMR components to three Li sites is confirmed by quantitative analysis of NMR spectra. Structural sites occupancy deduced by NMR spectroscopy coincides with that obtained by Rietveld analysis of ND patterns (Table S6). Five-fold LiO_5 coordinated sites allocated at the planes occupied by sodium (y/b = 0) affect Li-O bonds characteristics (Figure 8). Moreover, arrangement of Ti^{3+} cations with respect Li3 differs considerably from that adopted with respect Li2 ions, what could cause differences detected on paramagnetic shifts detected in both Li signals. To better explain these differences additional work is required.

Li mobility. The temperature dependence of Ti^{3+} magnetic moments makes the study of Li MAS-NMR spectra with temperature necessary. In samples heated at increasing temperatures, smaller changes detected on the position of ^{7}Li MAS-NMR components have been ascribed to changes of paramagnetic interactions (temperature dependence of Ti^{3+} magnetic moments), and bigger changes to Li motion averaging. This analysis was performed on $Li_{0.8}Na_2Ti_6O_{13}$ and $Li_{1.7}Na_2Ti_6O_{13}$ lithium inserted samples.

$Li_{0.8}Na_2Ti_6O_{13}$. Figure S4 shows the ^{7}Li MAS-NMR spectra of $Li_{0.8}Na_2Ti_6O_{13}$ recorded at increasing temperatures. Up to 110°C chemical shift of the Li signal remains practically constant at 0.4 ppm, observing a slight decrease on the linewidth of this signal (from 6.4 to 5.6 ppm). This component was ascribed to Li1 ions at 2*c* sites, far from paramagnetic Ti^{3+} centers, and located at the centre of conduction channels. The thermal evolution of ^{7}Li MAS-NMR spectra suggests that mobility of Li1 species is rather low. Similar conclusions were deduced from ^{23}Na MAS NMR spectra.

$Li_{1.7}Na_2Ti_6O_{13}$. The ^{23}Na MAS NMR spectrum of $Li_2Na_2Ti_6O_{13}$ shows an important paramagnetic broadening, however changes produced during heating were limited. In Li

inserted $Li_2Na_2Ti_6O_{13}$, besides the Li1 signal ascribed to 2*c* site, two new shifted components at ∼-10 and +40 ppm have been ascribed to Li2 and Li3 ions with different disposition with respect Ti^{3+} centers.

To analyze Li mobility, the temperature dependence of three detected components has been investigated (Figure 9a). The $Li_{1.7}Na_2Ti_6O_{13}$ sample used here corresponds to that used previously in ND experiments. The ^{7}Li MAS-NMR profile differs slightly from that described previously, indicating some dependence of site occupancies with thermal history. The linear variation observed on position of three components with inverse temperature has been ascribed to the decrease of paramagnetic interactions. From measured slopes it is possible to deduce hyperfine constants describing these interactions. The variation deduced for ~ -10 and +40 ppm components display different sign and slope, indicating that paramagnetic interactions differ, as discussed previously, in two environments (Figure 9b). Values of chemical shift, half height linewidth and area of each component are given as a function of the inverse temperature in Table S7.

The variation of linewidth of the three components differ considerably (Figure 9c). The linewidth of the Li3 component decreases considerably above 300K, indicating the onset of important motions that averages quadrupole Li-network and dipolar Li-Li and Li-Ti^{3+} interactions. Changes observed in linewidth of Li1 and Li2 ions are considerably lower, indicating a lower mobility. The temperature dependence of relative areas of three components displays considerable differences for three Li species (Figure 9d). Below 300K the amount of Li1 species decreases at the expense of Li3 content; however, for higher temperatures Li3 decreases, favoring the increment of (Li1+Li2) populations.

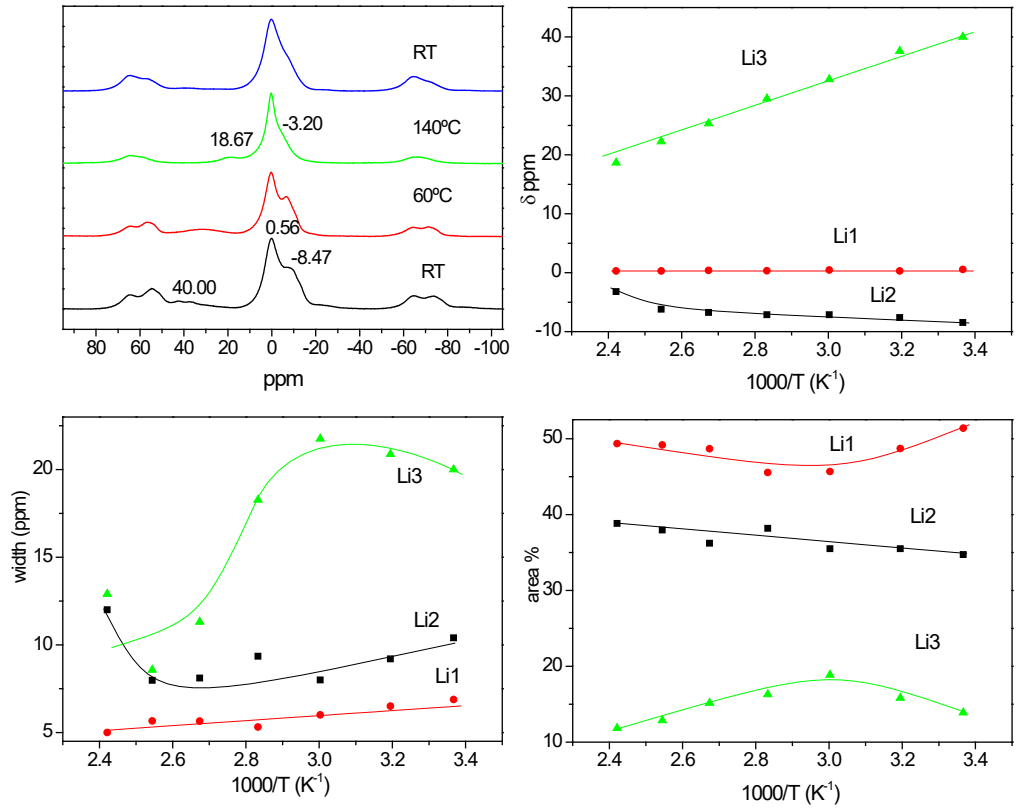

Figure 9. a) Evolution of ^{7}Li MAS-NMR spectra at increasing temperatures, Variation of b) position, c) line-width and d) relative area of three detected Li MAS-NMR components *vs.* inverse temperature.

In the case of the Li2 component, its position departs from the linear prediction above 120ºC, suggesting the onset of more important motions that average paramagnetic interactions. Deconvolution of Li MAS-NMR spectra shows the existence of local exchange between Li1 and Li2 at 130ºC, being its motion much less effective than Li3 species at this temperature.

4. Discussion

The allocation of Li in the structure of $Na_2Ti_6O_{13}$ requires reasonable Li-O bond distances and the minimization of electrostatic Li-Na and Li-Li repulsions. The lithium inserted at 1.4 V (x = 0.8) occupies Li1(2*c*) sites, allowing a suitable Li coordination

while electrostatic repulsions remain low. The partial filling of empty Li2(4*i*) tunnel sites is produced at 1.1 V during extensive lithium uptake (x > 1). In this case, the reversible Li transfer from the fully occupied 2*c* site to empty 4*i* sites allows the minimization of Li-Li interactions. To alleviate Li-Li interactions, lithium can alternatively occupy interstitial Li3(4*i)* sites, where lithium adopts a fivefold square pyramidal coordination. The proximity of Li3 sites to Na ions in the *y*/*b*=0 plane limits its occupancy. Finally, allocation of lithium at central 2*d* sites (sodium positions), where lithium would adopt an unusual LiO_8 coordination with large Li-O distances, cannot be produced**.**

***Li motion mechanism*.** In lithium inserted materials sodium atoms remain at the same site fixed sites, exerting a target effect, by which incoming Li ions are conducted to appropriate sites. In the case of Na cations, small chemical shifts in ^{23}Na MAS NMR spectra suggest that Na cations remain near Ti^{4+} cations. Concerning Li ions allocation, the overwhelming tetrahedral LiO_4 or octahedral LiO_6 coordination geometries in oxides are difficult to achieve in the tunnel structure of $Na_2Ti_6O_{13}$. In this compound Li-Na repulsions favor allocation of lithium at square planar LiO_4 sites with reasonable Li-O bond distances. The stabilization of Na at 4*i* sites favors the Li to be allocated at 2*c* sites.

Li insertion produces the reduction of titanium cations, increasing paramagnetic interactions between Li^+ and Ti^{3+} cations. These interactions decrease with increasing Li-Ti distance, making main changes detected in ^{7}Li MAS-NMR spectra be produced by Ti^{3+} cations at short distances (below 3 Å). From this fact, only Ti cations that share oxygen atoms with lithium (Ti-O-Li associations) will be considered. The Ti^{3+} magnetic moments are given by the expression

$$\mu_{eff} = \mu^2 \cdot B_0/3kT \qquad (2)$$

where μ_{eff} is the averaged magnetic moment observed by Li atoms, μ is the magnetic moment of Ti^{3+} cations and B_0 and T stand for external magnetic field and temperature. According to expression (2), paramagnetic interactions increase with magnetic field and decrease with temperature in NMR experiments.

During the first insertion step (1.35 V), lithium is allocated at square planar $Li1O_4$ (2*c* sites), maintaining low interactions with Na^+ ions. A schematic distribution of lithium along conduction paths has been elaborated taking into account results obtained from Fourier map differences (Figure 10a). Electrostatic Li1-Li2 repulsions makes the simultaneous occupation of Li1 and Li2 sites not favorable in $LiNa_2Ti_6O_{13}$. On the other hand, the partial occupation of Li3(4*i*) sites favors Li diffusion along the *b*-axis, following sinusoidal - Li1(2c) → Li3(4i) → Li1(2c) - paths (Figure 10b). In this motion, residence times at Li1 sites are considerably higher than at Li3 sites, making detection of lithium at these sites difficult.

During the second lithiation step (at 1.1 V), stabilization of two Li ions at *y*/*b*=0.5 planes requires some rearrangement of Li ions; in particular, electrostatic Li-Li repulsions favor the allocation of two Li ions at separated Li2(4*i*) positions (Figure 10b). In this case, isotropic paramagnetic interactions with Ti^{3+} allocated at Ti1 sites are important, and ^{7}Li MAS-NMR components are shifted from diamagnetic positions.

In $Li_{1.7}Na_2Ti_6O_{13}$ allocation of lithium at interstitial fivefold-coordinated Li3(4*i*) sites is possible, minimizing Li-Li repulsions. However, in this case Li-Na repulsions increase, impeding an important occupation of these sites. The partial occupation of Li1(2*c*) and Li3(4*i*) sites favors the mobility of lithium along Li1(2*c*) → Li3(4*i*) → Li1(2*c*) paths. The linear variation of the 40 ppm component position with inverse temperature, suggests that paramagnetic interactions with Ti^{3+} are also important.

Concerning signals at ~0.4 and -10 ppm (Li allocated at Li1 and Li2 sites), separation between lines decreases merging together at temperatures near 130ºC. The signal at -10 ppm departs from the linear variation with inverse temperature, indicating the existence of faster exchanges between Li1 and Li2 species than between Li1 and Li3 species. The variation of intensity of the three bands shows that the Li3 signal decreases but (Li1+Li2) increase with temperature, underlining a bad stabilization of lithium at Li3 sites. This fact favors Li motion along the *b*-axis.

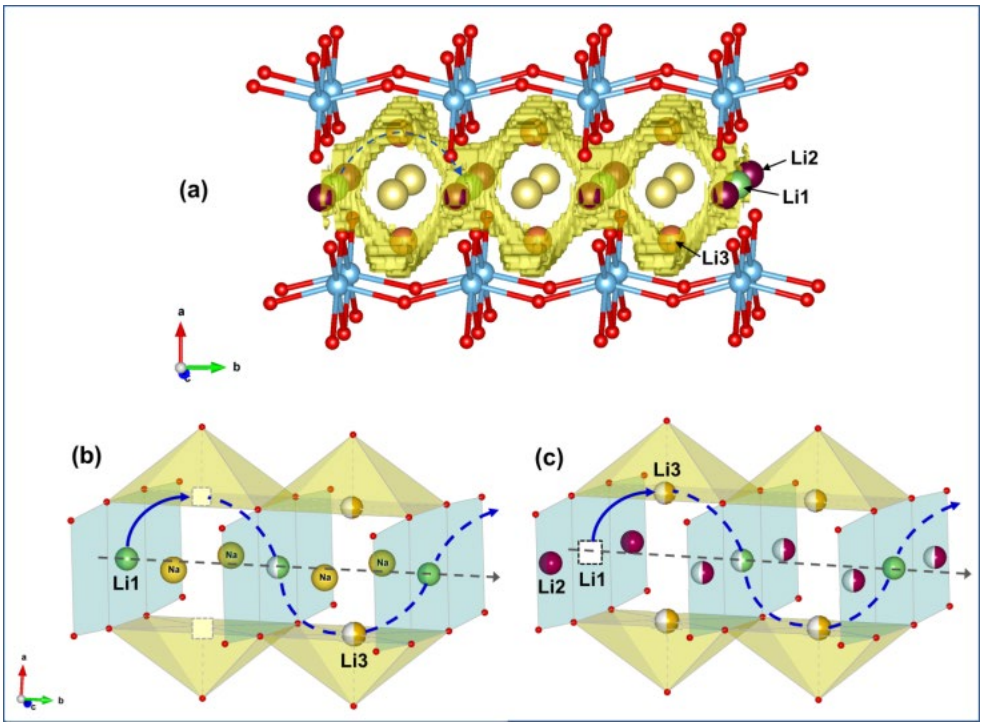

Figure 10. Lithium motion in $Li_xNa_2Ti_6O_{13}$. The Li sites and diffusion pathway as deduced from BVS isosurfaces of mobile lithium ions (yellow) overlaid on the structure along [010] (a). Schematic view of correlated Li motions produced in x = 0.8 (b) and x = 1.7 (c). Na atoms have been omitted in (c) for clarity. Key: Octahedral Ti (blue); O (red); Li1 (green); Li2 (red); Li3 (gold).

In summary, it can be concluded that Na ions force the Li ions to follow a sinusoidal - Li1(2*c*) → Li3(4*i*) → Li1(2*c*) –path motion through interstitial Li3(4*i*) sites. However, when the amount of Li increases, Li pairs can be formed at *y*/*b*=0, making the mobility of Li(2*c*) species lower. This arrangement reduces the amount of charge carriers involved in conduction processes. Electrostatic Li-Na repulsions impede extended lithiation of $Li_xNa_2Ti_6O_{13}$ samples.

5. Conclusions

Operando synchrotron X-ray diffraction measurements were performed to investigate the lithium insertion mechanism in $Na_2Ti_6O_{13}$. Fourier map differences performed on ND patterns of pristine and lithiated $Na_2Ti_6O_{13}$ samples allowed Li and Na positions to be deduced. In $Li_{0.8}Na_2Ti_6O_{13}$, lithium is located at Li1(2*c*) sites, but in $Li_{1.7}Na_2Ti_6O_{13}$ lithium resides at Li2 and Li3 (both 4*i*) besides Li1 (2*c*) sites. In this analysis Ti^{3+} sites were preferentially allocated at Ti1 and paramagnetic shifts of ^{7}Li MAS-NMR components were justified on the basis of Li^+-Ti^{3+} distances. A careful analysis of structural information deduced by neutron diffraction made it possible to identify conduction paths in lithium inserted samples. During the first insertion stage (at 1.35 V) lithium is allocated at square planar $Li1O_4$ (2*c*) sites, minimizing electrostatic repulsions with Na ions. The filling of Li2(4*i*) sites, by transfer from 2*c* sites, starts during lithium uptake in $Li_{0.8}Na_2Ti_6O_{13}$. The allocation of two lithium ions at y/b=0.5 planes decreases Li mobility by increasing correlation effects on Li motions. Long term motions are favored by partial occupation of interstitial Li3(4*i*) sites; however, the proximity of Li to Na ions limits Li insertion to ca. 2 Li ions/ structural formula. In $Li_{1.7}Na_2Ti_6O_{13}$ stabilization of lithium at Li2 and Li3 sites is difficult, making that occupation of these sites remain always partial.

A model for lithium distribution was elaborated considering Li site occupations deduced from Rietveld and NMR quantitative analyses in $Li_{0.8}Na_2Ti_6O_{13}$ and $Li_{1.7}Na_2Ti_6O_{13}$ samples. In this model most probable - Li1(2c) → Li3(4i) → Li1(2c) - conduction paths were deduced. The Li mobility has been followed by ^{7}Li MAS-NMR spectra recorded at increasing temperatures. The ^{23}Na MAS-NMR analysis showed that Na cations always remain at specific sites, but Li ions move along sinusoidal paths to reduce Li-Na electrostatic interactions. Formation of Li pairs at y/b=0 planes reduces the amount of mobile Li ions that participate in conduction processes.

Author Information

Corresponding Author

akuhn@ceu.es

Conflicts of interest

There are no conflicts of interest to declare.

Acknowledgment

This work has been founded by Spanish projects MINECO MAT2013-46452-C4-1,2-R and MATERYENER3-CM (S20132/MIT-2753).

References

(1) Williard, N.; He, W.; Hendricks, C.; Pecht, M. Lessons Learned from the 787 Dreamliner Issue on Lithium-Ion Battery Reliability. *Energies* **2013**, 6, 4682-4689.

(2) Suresh, P.; Shukla, A. K.; Shivashankar, S. A.; Munichandraiah, N. Rechargeable Lithium Cells with Dendrite-free electrodeposited Lithium on Aluminium as Negative Electrode. *Journal of Power Sources* **2004**, 132, 166-171.

(3) Li, Z.; Huang, J.; Yann Liaw, B.; Metzler, V.; Zhang, J. A Review of Lithium Deposition in Lithium-ion and Lithium Metal secondary Batteries. *Journal of Power Sources* **2014**, 254, 168-182.

(4) Lanz, M.; Novák, P. DEMS Study of Gas Evolution at thick Graphite Electrodes for Lithium-ion Batteries: the Effect of γ-butyrolacton. *Journal of Power Sources* **2001**, 102, 277-282.

(5) Bugga, R. V.; Smart, M. C. Lithium Plating Behavior in Lithium-Ion Cells. *ECS Transactions* **2010**, 25, 241-252.

(6) Leising, R. A.; Palazzo, M. J.; Takeuchi, E. S.; Takeuchi, K. J. A Study of the Overcharge Reaction on Lithium-ion Batteries. *Journal of Power Sources* **2001**, 97–98, 681-683.

(7) Thackeray, M. M.; Johnson, P. J.; de Picciotto, L. A.; Bruce, P. G.; Goodenough, J. B. Electrochemical Extraction of Lithium from $LiMn_2O_4$. *Materials Research Bulletin* **1984**, 19, 179-187.

(8) Rossen, E.; Reimers, J. N.; Dahn, J. R. Synthesis and Electrochemistry of Spinel LT-$LiCoO_2$. *Solid State Ionics* **1993**, 62, 53-60.

(9) Thackeray, M. M.; David, W. I. F.; Bruce, P. G.; Goodenough, J. B. Lithium Insertion into Manganese Spinels. *Materials Research Bulletin* **1983**, 18, 461-472.

(10) Fauteux, D.; Koksbang, R. J. Rechargeable Lithium Battery Anodes: alternatives to metallic Lithium. *Appl Electrochem* **1993**, 23, 1-10.

(11) Gibbard, H. F. Seventh International meeting on lithium batteries: extended abstracts and program, Boston, Massachusetts, USA, May 15-20, **1994**, 1994.

(12) Ohzuku, T.; Ueda, A.; Yamamoto, N. Zero-Strain Insertion Material of $Li[Li_{1/3}Ti_{5/3}]O_4$ for Rechargeable Lithium Cells. *Journal of The Electrochemical Society* **1995**, 142, 1431-1435.

(13) Jung, H.-G.; Jang, M. W.; Hassoun, J.; Sun, Y.-K.; Scrosati, B. A high-rate long-life $Li_4Ti_5O_{12}/Li[Ni_{0.45}Co_{0.1}Mn_{1.45}]O_4$ Lithium-ion Battery. *Nat Commun* **2011**, 2, 516

(14) Zhao, L.; Hu, Y.-S.; Li, H.; Wang, Z.; Chen, L. Porous $Li_4Ti_5O_{12}$ Coated with N-Doped Carbon from Ionic Liquids for Li-Ion Batteries. *Advanced Materials* **2011**, 23, 1385-1388.

(15) Patoux, S.; Masquelier, C. Lithium Insertion into Titanium Phosphates, Silicates, and Sulfates. *Chemistry of Materials* **2002**, 14, 5057-5068.

(16) Yang, Z.; Choi, D.; Kerisit, S.; Rosso, K. M.; Wang, D.; Zhang, J.; Graff, G.; Liu, J. Nanostructures and Lithium Electrochemical Reactivity of Lithium Titanites and Titanium Oxides: A review. *Journal of Power Sources* **2009**, 192, 588-598.

(17) Liu, Y.; Yang, Y. Recent Progress of TiO_2-Based Anodes for Li Ion Batteries. *Journal of Nanomaterials* **2016**, 2016, Article ID 8123652 (15 pages).

(18) Chiba, K.; Kijima, N.; Takahashi, Y.; Idemoto, Y.; Akimoto, J. Synthesis, Structure, and Electrochemical Li-ion Intercalation Properties of $Li_2Ti_3O_7$ with $Na_2Ti_3O_7$-type Layered Structure. *Solid State Ionics* **2008**, 178, 1725-1730.

(19) Dominko, R.; Baudrin, E.; Umek, P.; Arcon, D.; Gaberscek, M.; Jamnik, J. Reversible Lithium Insertion into $Na_2Ti_6O_{13}$ Structure. *Electrochemistry Communications* **2006**, 8, 673-677.

(20) Dominko, R.; Dupont, L.; Gaberšček, M.; Jamnik, J.; Baudrin, E. Alkali Hexatitanates-$A_2Ti_6O_{13}$ (A = Na, K) as Host Structure for Reversible Lithium Insertion. *Journal of Power Sources* **2007**, 174, 1172-1176.

(21) Garnier, S.; Bohnke, C.; Bohnke, O.; Fourquet, J. L. Electrochemical Intercalation of Lithium into the Ramsdellite-Type Structure of $Li_2Ti_3O_7$. *Solid State Ionics* **1996**, 83, 323-332.

(22) Perez-Flores, J. C.; Baehtz, C.; Hoelzel, M.; Kuhn, A.; Garcia-Alvarado, F. Full Structural and Electrochemical Characterization of $Li_2Ti_6O_{13}$ as Anode for Li-ion Batteries. *Physical Chemistry Chemical Physics* **2012**, 14, 2892-2899.

(23) Perez-Flores, J. C.; Baehtz, C.; Hoelzel, M.; Kuhn, A.; Garcia-Alvarado, F. $H_2Ti_6O_{13}$, a New Protonated Titanate Prepared by Li^+/H^+ Ion Exchange: Synthesis, Crystal Structure and Electrochemical Li Insertion Properties. *RSC Advances* **2012**, 2, 3530-3540.

(24) Perez-Flores, J. C.; Garcia-Alvarado, F.; Hoelzel, M.; Sobrados, I.; Sanz, J.; Kuhn, A. Insight into the Channel Ion Distribution and Influence on the Lithium Insertion Properties of Hexatitanates $A_2Ti_6O_{13}$ (A = Na, Li, H) as Candidates for Anode Materials in Lithium-ion Batteries. *Dalton Transactions* **2012**, 41, 14633-14642.

(25) Torres-Martínez, L. M.; Juárez-Ramírez, I.; Del Ángel-Sánchez, K.; Garza-Tovar, L.; Cruz-López, A.; Del Ángel, G. Rietveld Refinement of Sol–Gel $Na_2Ti_6O_{13}$ and its Photocatalytic Performance on the Degradation of Methylene Blue. *Journal of Sol-Gel Science and Technology* **2008**, 47, 158-164.

(26) Andersson, S.; Wadsley, A. D. The structures of $Na_2Ti_6O_{13}$ and $Rb_2Ti_6O_{13}$ and the Alkali Metal Titanates. *Acta Crystallographica* **1962**, 15, 194-201.

(27) Y. Wang, H. Zhang, X. Yao, H. Zhao. Theoretical Understanding and Prediction of Lithiated Sodium Hexatitanates. ACS Appl. Mater. Interfaces 2013, 5, 1108−1112.

(28) Li, P.; Wang, P.; Qian, S.; Yu, H.; Lin, X.; Shui, M.; Zheng, X.; Long, N.; Shu, J. Synthesis of $Na_2Ti_6O_{13}$ Nanorods as Possible Anode Materials for Rechargeable Lithium Ion Batteries. *Electrochimica Acta* 2016, 187, 46-54.

(29) Pérez-Flores, J. C.; Kuhn, A.; García-Alvarado, F. Synthesis, Structure and Electrochemical Li Insertion Behaviour of $Li_2Ti_6O_{13}$ with the $Na_2Ti_6O_{13}$ Tunnel-Structure. *Journal of Power Sources* **2011**, 196, 1378-1385.

(30) Perez-Flores, J. C.; Baehtz, C.; Kuhn, A.; Garcia-Alvarado, F. Hollandite-type TiO_2: a New Negative Electrode Material for Sodium-ion Batteries. *Journal of Materials Chemistry A* **2014**, 2, 1825-1833.

(31) M. Bianchini, F. Fauth,N. Brisset, F. Weill, E. Suard, C. Masquelier, L. Croguennec. Comprehensive Investigation of the Na3V2(PO4)2F3−NaV2(PO4)2F3 System by Operando High Resolution Synchrotron X-ray Diffraction. Chem. Mater. 2015, 27, 3009−3020.

(32) Rodriguez-Carvajal, J. Recent Advances in Magnetic Structure Determination by Neutron Powder Diffraction. *Physica B: Condensed Matter* **1993**, 192, 55-69.

(33) Rietveld, H. The Crystal structure of Some Alkaline Earth Metal Uranates of the Type M_3UO_6. *Acta Crystallographica* **1966**, 20, 508-513.

(34) Rietveld, H. Line Profiles of Neutron Powder-Diffraction Peaks for Structure Refinement. *Acta Crystallographica* 1967, 22, 151-152.

(35) Sears, V. F. Neutron Scattering Lengths and Cross Sections. *Neutron News* **1992**, 3, 26-37.

(36) Momma, K.; Izumi, F. VESTA 3 for Three-Dimensional Visualization of Crystal, Volumetric and Morphology Data. *Journal of Applied Crystallography* **2011**, 44, 1272-1276.

(37) Grey, C. P.; Dupré, N. NMR Studies of Cathode Materials for Lithium-Ion Rechargeable Batteries. *Chemical Reviews* **2004**, 104, 4493-4512.

(38) Shen, K.; Wagemaker, M. $Na_{2+x}Ti_6O_{13}$ as Potential Negative Electrode Material for Na-Ion Batteries. *Inorganic Chemistry* **2014**, 53, 8250-8256.

(39) M. Wagemaker, D. R. Simon, E. M. Kelder, J. Schoonman, C. Ringpfeil, U. Haake, D. Lützenkirchen-Hecht, R. Frahm, F. M. Mulder. A Kinetic Two-Phase and Equilibrium Solid Solution in Spinel $Li_{4+x}Ti_5O_{12}$. *Adv. Mater.* 2006, *18*, 3169–3173.

(40) Bianchini, M.; Ateba-Mba, J. M.; Dagault, P.; Bogdan, E.; Carlier, D.; Suard, E.; Masquelier, C.; Croguennec, L. Multiple phases in the ε-VPO_4O–$LiVPO_4O$–Li_2VPO_4O system: a combined solid state electrochemistry and diffraction structural study. *J. Mater. Chem. A* 2014, 2, 10182-10192.

(41) Zhang, X.; van Hulzen, M.; Singh, D. P.; Brownrigg, A.; Wright, J. P.; van Dijk, N. H.; Wagemaker, M. Rate-Induced Solubility and Suppression of the First-Order Phase Transition in Olivine $LiFePO_4$. *Nano Lett.* 2014, 14, 2279-2285.

(42) Rodríquez-Carvajal, J. Magnetic Structure Determination from Powder Diffraction Symmetry Analysis and Simulated Annealing. *Materials Science Forum* **2001**, 378, 268-273.

(43) Kataoka, K.; Awaka, J.; Kijima, N.; Hayakawa, H.; Ohshima, K.-i.; Akimoto, J. Ion-Exchange Synthesis, Crystal Structure, and Electrochemical Properties of $Li_2Ti_6O_{13}$. *Chemistry of Materials* **2011**, 23, 2344-2352.

Insert Table of Contents artwork here